



NIR-enhanced Pt single atom/g-C₃N₄ nanozymes as SOD/CAT mimics to rescue ATP energy crisis by regulating oxidative phosphorylation pathway for delaying osteoarthritis progression

Jianhui Xiang^{a,c}, Xin Yang^a, Manli Tan^a, Jianfeng Guo^a, Yuting Ye^a, Jiejia Deng^a, Zhangrui Huang^b, Hanjie Wang^b, Wei Su^a, Jianwen Cheng^c, Li Zheng^{a,*}, Sijia Liu^{a,**}, Jingping Zhong^{a,***}, Jinmin Zhao^{a,b,c}

^a Guangxi Engineering Center in Biomedical Material for Tissue and Organ Regeneration, Collaborative Innovation Centre of Regenerative Medicine and Medical BioResource Development and Application Co-constructed By the Province and Ministry, Guangxi Key Laboratory of Regenerative Medicine, The First Affiliated Hospital of Guangxi Medical University, No. 6 Shuangyong Road, Nanning, Guangxi 530021, PR China

^b Life Sciences Institute, Guangxi Medical University, No. 22 Shuangyong Road, Nanning, Guangxi, 530021, PR China

^c Department of Orthopaedics Trauma and Hand Surgery, The First Affiliated Hospital of Guangxi Medical University, No. 6 Shuangyong Road, Nanning, Guangxi, 530021, PR China

ARTICLE INFO

Keywords:

ATP energy crisis
Osteoarthritis progression
Oxidative phosphorylation pathway
Nanozymes

ABSTRACT

Osteoarthritis (OA) progresses due to the excessive generation of reactive oxygen and nitrogen species (ROS/RNS) and abnormal ATP energy metabolism related to the oxidative phosphorylation pathway in the mitochondria. Highly active single-atom nanozymes (SAzymes) can help regulate the redox balance and have shown their potential in the treatment of inflammatory diseases. In this study, we innovatively utilised ligand-mediated strategies to chelate Pt⁴⁺ with modified g-C₃N₄ by π - π interaction to prepare g-C₃N₄-loaded Pt single-atom (Pt SA/C₃N₄) nanozymes that serve as superoxide dismutase (SOD)/catalase (CAT) mimics to scavenge ROS/RNS and regulate mitochondrial ATP production, ultimately delaying the progression of OA. Pt SA/C₃N₄ exhibited a high loading of Pt single atoms (2.45 wt%), with an excellent photothermal conversion efficiency (54.71%), resulting in tunable catalytic activities under near-infrared light (NIR) irradiation. Interestingly, the Pt-N₆ active centres in Pt SA/C₃N₄ formed electron capture sites for electron holes, in which g-C₃N₄ regulated the d-band centre of Pt, and the N-rich sites transferred electrons to Pt, leading to the enhanced adsorption of free radicals and thus higher SOD- and CAT-like activities compared with pure g-C₃N₄ and g-C₃N₄-loaded Pt nanoparticles (Pt NPs/C₃N₄). Based on the use of H₂O₂-induced chondrocytes to simulate ROS-injured cartilage *in vitro* and an OA joint model *in vivo*, the results showed that Pt SA/C₃N₄ could reduce oxidative stress-induced damage, protect mitochondrial function, inhibit inflammation progression, and rebuild the OA microenvironment, thereby delaying the progression of OA. In particular, under NIR light irradiation, Pt SA/C₃N₄ could help reverse the oxidative stress-induced joint cartilage damage, bringing it closer to the state of the normal cartilage. Mechanistically, Pt SA/C₃N₄ regulated the expression of mitochondrial respiratory chain complexes, mainly NDUFB2 of complex I and MT-ATP6 of ATP synthase, to reduce ROS/RNS and promote ATP production. This study provides novel insights into the design of artificial nanozymes for treating oxidative stress-induced inflammatory diseases.

1. Introduction

Osteoarthritis (OA) is a chronic degenerative joint disease and is the

main cause of disability in the elderly [1,2]. As OA progresses, joint replacement surgery becomes necessary given the lack of effective therapeutics [3]. Excessive reactive oxygen species (ROS) and active nitrogen species (RNS) are among the leading causes of OA. ROS/RNS

Peer review under responsibility of KeAi Communications Co., Ltd.

* Corresponding author.

** Corresponding author.

*** Corresponding author.

E-mail addresses: zhengli224@163.com (L. Zheng), heming_liu@163.com (S. Liu), jingpingzhong@163.com (J. Zhong).

<https://doi.org/10.1016/j.bioactmat.2024.02.018>

Received 23 November 2023; Received in revised form 13 February 2024; Accepted 14 February 2024

Available online 21 February 2024

2452-199X/© 2024 The Authors. Publishing services by Elsevier B.V. on behalf of KeAi Communications Co. Ltd. This is an open access article under the CC BY-NC-ND license (<http://creativecommons.org/licenses/by-nc-nd/4.0/>).

Abbreviations

CAT	catalase
DFT	density functional theory
EXAFS	extended X-ray absorption fine structure
ICP	inductively coupled plasma
HRP	natural horseradish peroxidase
NIR	near-infrared light
OA	osteoarthritis
PDOS	partial density of states
ROS/RNS	reactive oxygen and nitrogen species
SA	single-atom
SOD	superoxide dismutase
XAS	X-ray absorption spectroscopy
XPS	X-ray photoelectron spectroscopy

trigger oxidative stress that leads to irreversible damage, ATP energy crisis, and cell apoptosis [4,5]. During OA progression, ROS/RNS are closely related to the respiratory electron transfer chain pathway of oxidative phosphorylation in the mitochondria, which regulates not only the redox balance of the microenvironment but also ATP energy metabolism [6,7]. Therefore, eliminating excessive ROS/RNS and regulating mitochondrial ATP production may effectively inhibit oxidative stress and rescue chondrocyte apoptosis in the treatment of OA [8,9].

Recently, biocompatible nanozymes (such as platinum, cerium dioxide, iron, and redox polymers) that can mimic natural superoxide dismutase (SOD) and catalase (CAT), which can effectively eliminate ROS, have been used in OA therapy [10,11]. Among the various nanozymes, Pt-based nanoparticle (NP) nanozymes have attracted significant attention in biomedicine, diagnosis, and disease treatment owing to their excellent multi-enzyme-mimicking properties (such as for SOD and CAT), biosafety, simplicity and controllability of synthesis, and stability *in vivo* [12–14]. However, only the surface Pt atoms of Pt NPs are involved in enzymatic catalysis, leading to a low atomic utilisation rate and ultimately limited catalytic activity. Increasing the Pt content may enhance the catalytic activity, though biological safety is compromised due to the cytotoxicity of Pt. Therefore, improving the atomic utilisation rate of Pt is crucial for enhancing the enzymatic activity of Pt NPs [15, 16]. Research on single-atom (SA) nanozymes with a 100% atom utilisation rate, rich active sites, high selectivity, and perfect matching with natural enzymes can help provide novel insights into the construction of highly bioactive Pt NPs [17–20]. However, for Pt SA-based NPs, suitable carrier materials that can control the bonding/coordination between individual atoms and carriers to compensate for the increasing surface energy of the atom have yet to be exploited [21,22].

Graphitic carbon nitride ($g\text{-C}_3\text{N}_4$) is highly recommended to capture isolated SAs because of the uniform and rich N/C coordination framework formed by the unique triazine structure [23,24]. Specifically, the interlayer distance of $g\text{-C}_3\text{N}_4$ facilitates the preferential adsorption of metal atoms onto triangular pores to react with its rich pyridine nitrogen active sites to form bonds, thereby promoting effective coordination of metal SAs [25,26]. The unique six pairs of lone nitrogen electrons in $g\text{-C}_3\text{N}_4$ can enhance metal-carrier interaction, further improving the catalytic activity [27]. Moreover, $g\text{-C}_3\text{N}_4$ exhibits excellent optical and electronic properties [28]. Combining precious metals with $g\text{-C}_3\text{N}_4$ can help form a space charge separation region (also known as the Schottky barrier), which can develop as an electron hole that serves as an effective electron capture site to further improve the photocatalytic activity [29, 30]. Roy et al. reported that $g\text{-C}_3\text{N}_4$, as a carrier for Cu SA, regulated the d-band centre shift of Cu and enhanced the intermediate binding energy, which was beneficial for improving the photo-oxidation performance [31]. Ding et al. constructed In SAs on $g\text{-C}_3\text{N}_4$, forming In–N₄ active

sites, resulting in the reduced (002) crystal plane spacing of $g\text{-C}_3\text{N}_4$, which remarkably improved the reaction activity of CO₂ photoreduction [32]. Jiang et al. developed a highly active and stable $g\text{-C}_3\text{N}_4$ -supported Ag SA catalyst (Ag–N₂C₂/CN), which can extend the light absorption range and improve charge transfer, thereby improving the catalytic activity [33]. Hence, $g\text{-C}_3\text{N}_4$ may be an excellent carrier for Pt SA, as it can potentially enhance the SOD/CAT enzymatic activity, though there have been no reports on its usage.

In this study, we innovatively designed $g\text{-C}_3\text{N}_4$ -supported Pt SA catalysts (Pt SA/C₃N₄) that serve as SOD/CAT mimics with an enzymatic activity that is tunable by NIR light irradiation, in an attempt to scavenge ROS/RNS and regulate mitochondrial ATP production, thereby alleviating the progression of OA (Fig. 1). Specifically, ligand-mediated strategies were utilised to chelate Pt⁴⁺, followed by $\pi\text{-}\pi$ interaction with the modified $g\text{-C}_3\text{N}_4$, to prepare high-loading Pt SA nanozymes. The Pt–N₆ active centres in Pt SA/C₃N₄ formed electron capture sites for electron holes, in which $g\text{-C}_3\text{N}_4$ regulated the d-band centre of Pt, and the N-rich sites transferred electrons to Pt, resulting in the enhanced adsorption of free radicals and thus excellent SOD/CAT-like activity. NIR light irradiation was employed to modulate the catalytic activity of Pt SA/C₃N₄ via photothermal conversion. Based on H₂O₂-induced chondrocytes and an animal joint model of OA, Pt SA/C₃N₄, particularly under NIR II irradiation, could effectively scavenge ROS/RNS, reduce oxidative stress-induced damage, protect mitochondrial function, inhibit the inflammatory response, further rebuild the OA microenvironment, and ultimately delay OA progression. Mechanistically, Pt SA/C₃N₄ regulated the expression of mitochondrial respiratory chain complexes to reduce ROS/RNS and rescue the ATP energy crisis.

2. Results and discussion

2.1. Preparation and characterization of Pt SA/C₃N₄ nanozymes

Fig. 1 shows the methodology for synthesising the Pt SA/C₃N₄ nanozymes. We prepared $g\text{-C}_3\text{N}_4$ -loaded Pt SAs (Pt SA/C₃N₄) using 1,10-phenanthroline coordinated Pt atoms and a positively charged thin sheet of carbon nitride ($g\text{-C}_3\text{N}_4$) through one-step thermal annealing. The transmission electron microscopy (TEM) image revealed a 2D porous sheet of Pt SA/C₃N₄ (Fig. 2a) similar to the $g\text{-C}_3\text{N}_4$ sheet (Fig. S1a), with no evident nanoparticles on the surface, unlike the Pt NPs (Fig. S1b). However, in the aberration-corrected high-angle annular dark-field scanning TEM (AC-HAADF STEM) image, Pt SAs can be observed, indicated by green circles (Fig. 2b and c). Energy dispersive spectrometry (EDS) mapping revealed uniformly dispersed C, N, O, and Pt on Pt SA/C₃N₄ (Fig. 2d, e, and Fig. S2), and an inductively coupled plasma (ICP) test showed a Pt content of 2.45 wt%, demonstrating the successful synthesis of the Pt SAs. And the morphology of Pt SA/C₃N₄ remained unchanged under physiological conditions such as synovial fluid. (Fig. S3). In the X-ray diffraction (XRD) pattern (Fig. 2f), except for Pt NPs/C₃N₄, neither Pt SA/C₃N₄ nor $g\text{-C}_3\text{N}_4$ exhibited crystal plane diffraction peaks characteristic of Pt. The unique s-triazine ring structure of $g\text{-C}_3\text{N}_4$ can be observed in the infrared spectra (Fig. S4). In addition, Pt SA/C₃N₄ was positively charged, which is beneficial for allowing cells that are negatively charged (Fig. S5).

X-ray photoelectron spectroscopy (XPS) was employed to examine the electrical structure of the Pt SA/C₃N₄ nanozymes. The binding states of C, N, O, and Pt were found on Pt SA/C₃N₄ (Table S1). The high-resolution C 1s spectra of Pt SA/C₃N₄ matched four peaks at 284.6 (C=C), 285.5 (C–O–C), 286.7 (C–N), and 288.3 (C=O) (Fig. 2g). The high-resolution spectra of N1s were fitted to obtain three peaks at 398.6, 399.7, and 400.9 eV, corresponding to pyridine N, Pt–N, and graphite N, respectively (Fig. 2h). The fitted Pt 4f yielded Pt⁰ peaks (4f7/2 at 72.5 eV, 4f5/2 at 76.0 eV) and Pt²⁺ peaks (4f7/2 at 73.2 eV, 4f5/2 at 76.7 eV) (Fig. 2j). The high-resolution spectral-fitted peaks of C 1s, N 1s, and Pt 4f in Pt SA/C₃N₄ shifted compared with that in the case of Pt NPs, because of the high surface energy of the Pt SAs and electron transfer interactions

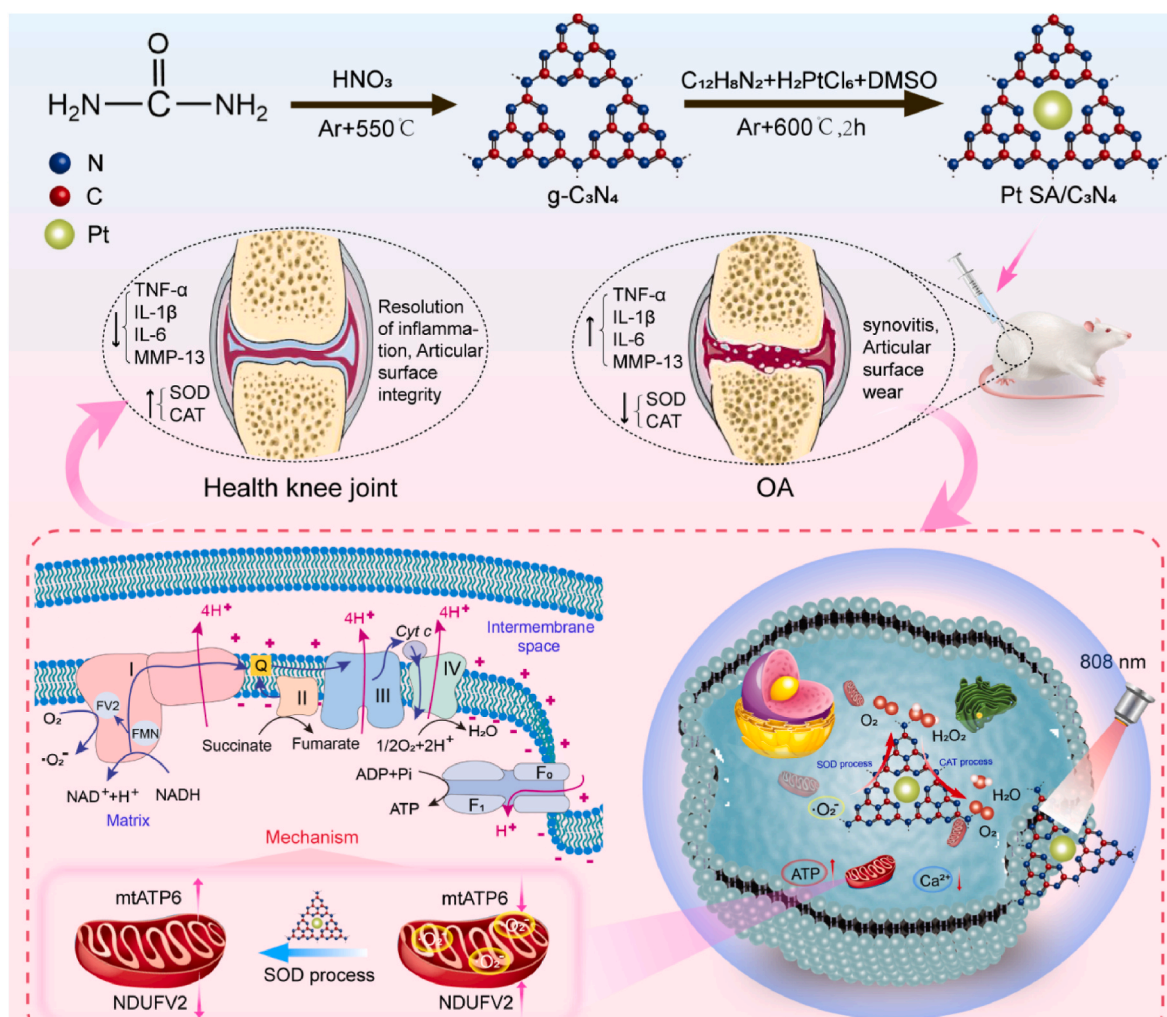


Fig. 1. The manufacture of Pt SA/C₃N₄ nanozymes and the fundamentals of biomimetic SOD and CAT for the scavenging of ROS.

with the surrounding elements, which is beneficial for enhancing the catalytic performance (Fig. 2j, Fig. S6).

The chemical structures of the Pt SA/C₃N₄ nanozymes were analysed by X-ray absorption spectroscopy (XAS). Fig. 2k shows the Pt K-edge XANES spectra of the absorption edge of Pt SA/C₃N₄ between the Pt foil and PtO₂, indicating that the valence of Pt is between those of Pt⁰ and Pt⁴⁺. The Fourier transform (FT) k³-weighted extended X-ray absorption fine structure (EXAFS) spectrum of Pt SA/C₃N₄ (Fig. 2l, Table S2) showed the same peak of PtO₂ at approximately 1.6 nm, corresponding to the Pt–N bond. The spectrum of Pt SA/C₃N₄ showed no Pt–Pt bond peaks near 2.5 nm in the Pt foil. Furthermore, as shown in Fig. 2m, the Pt K-edge EXAFS spectra of Pt SA/C₃N₄ well fit with the Pt–N₆ bond. To obtain convincing results, we present the wavelet transform (WT) contour maps of the three materials (Fig. 2n–p). Clearly, the maximum strength of Pt SA/C₃N₄ (4.3 Å⁻¹) is close to that of PtO₂ (5.5 Å⁻¹), which belongs to the Pt–N bond. Moreover, no Pt–Pt signal was detected in Pt SA/C₃N₄, whereas it was observed in the Pt foil (10.1 Å⁻¹), which is further proof of the dispersion of Pt SAs in Pt SA/C₃N₄.

2.2. Testing Pt SA/C₃N₄ nanozymes for natural enzyme-like activity

Owing to the potent electron supplementation effect of the Pt SA/C₃N₄ nanozymes produced by multi-element co-doping, these nanozymes are expected to help remove O₂^{•-} and •OH, and convert them into O₂ to simulate the activity of natural SOD and CAT enzymes.

As shown in Fig. S7, both the Pt NPs/C₃N₄ and Pt SA/C₃N₄

nanozymes exhibit dose-dependent SOD-like activity, whereas pure g-C₃N₄ does not. Pt SA/C₃N₄ exhibited a higher SOD-like activity than Pt NPs/C₃N₄, suggesting that the synergistic action of Pt atoms with g-C₃N₄ is a major factor in improving the SOD-like activity. These results can be further confirmed by the electron spin resonance (ESR) spectroscopy assay, which showed that Pt SA/C₃N₄ had the highest activity (Fig. 3d). This indicates that the atomic content of Pt, as an active site, may enhance the enzymatic activity. For Pt-based nanozymes, Pt SAs loaded on the basis of C and N are preferable for effectively improving the SOD-like activity because of their geometric and electronic matching with the structure of natural SOD (Fig. S8).

CAT, which is an important enzyme that catalyses the decomposition of H₂O₂ in organisms, also plays a key role in scavenging ROS, which are the main inducers of oxidative damage. From Fig. S9, we find that both the Pt NPs/C₃N₄ and Pt SA/C₃N₄ nanozymes exhibit dose-dependent CAT-like activity, except for pure g-C₃N₄. Compared with Pt NPs/C₃N₄, Pt SA/C₃N₄ has a 56% higher CAT-like activity, indicating that the electron transfer between the C, N, and Pt atoms helped significantly increase the CAT-like activity. Notably, with the continuous addition of H₂O₂, Pt SA/C₃N₄ decomposed H₂O₂ at the same rate (Fig. 3a–c, Fig. S10), indicating a stable and sustained CAT-like activity. In addition, Pt SA/C₃N₄ nanozymes still had stable CAT/SOD-like activity in the synovial fluid of SD rats (Fig. S11). Further, Pt SA/C₃N₄ nanozymes showed superior CAT-like and SOD-like activities compared with natural horseradish peroxidase (HRP) (Fig. S12). The ESR analysis also confirmed the potent CAT/SOD-like activity of Pt SA/C₃N₄ in

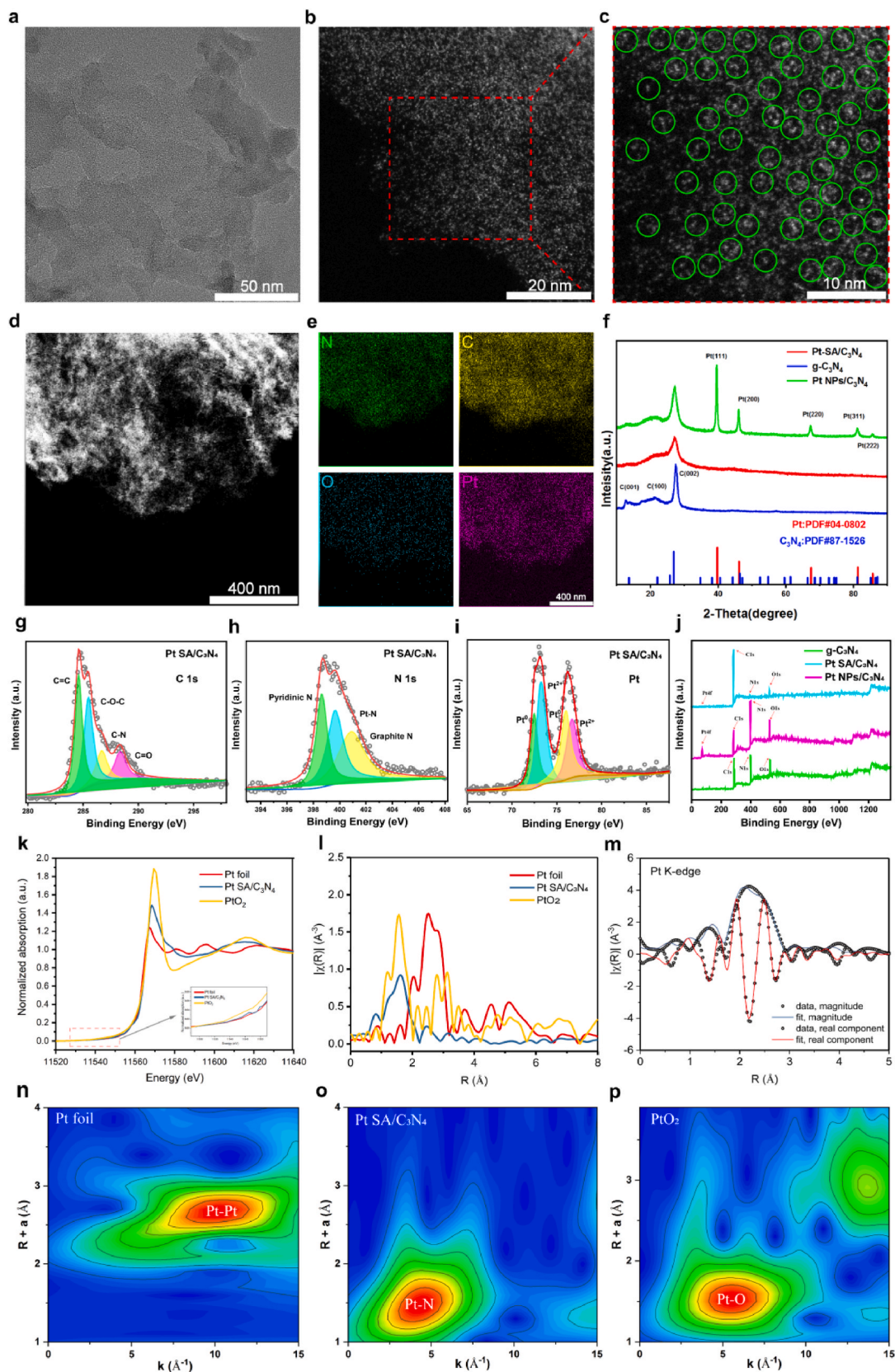


Fig. 2. Characterization of Pt SA/C₃N₄ nanozymes. (a) Pt SA/C₃N₄ TEM (a) and HAADF-STEM (b) images, scale bars: 50 nm for a and 20 nm for b. (c) Aberration-corrected HAADF-STEM (AC-HAADF-STEM) of Pt SA/C₃N₄ with different magnifications, Scale bar: 10 nm, wherein bright dots represent Pt SA/C₃N₄ single atom centres. (d) High-angle-annular dark-field scanning TEM (HAADF-STEM) and (e) element mapping images of Pt SA/C₃N₄, and scale bar: 400 nm; Pt NPs/C₃N₄ and Pt SA/C₃N₄ nanozymes. (f) XRD of g-C₃N₄, Pt NPs/C₃N₄ and Pt SA/C₃N₄ nanozymes. (g–j) XPS spectra at high resolution of Pt SA/C₃N₄ nanozymes. (k) Pt K-edge XANES spectra of several materials, (l) k²-weighted $\chi(k)$ Fourier transformed EXAFS function spectra of different samples. (m) Pt K-edge EXAFS fitting spectra of Pt SA/C₃N₄ in R-space. (n–p) WT images at the Pt K-edge of different samples.

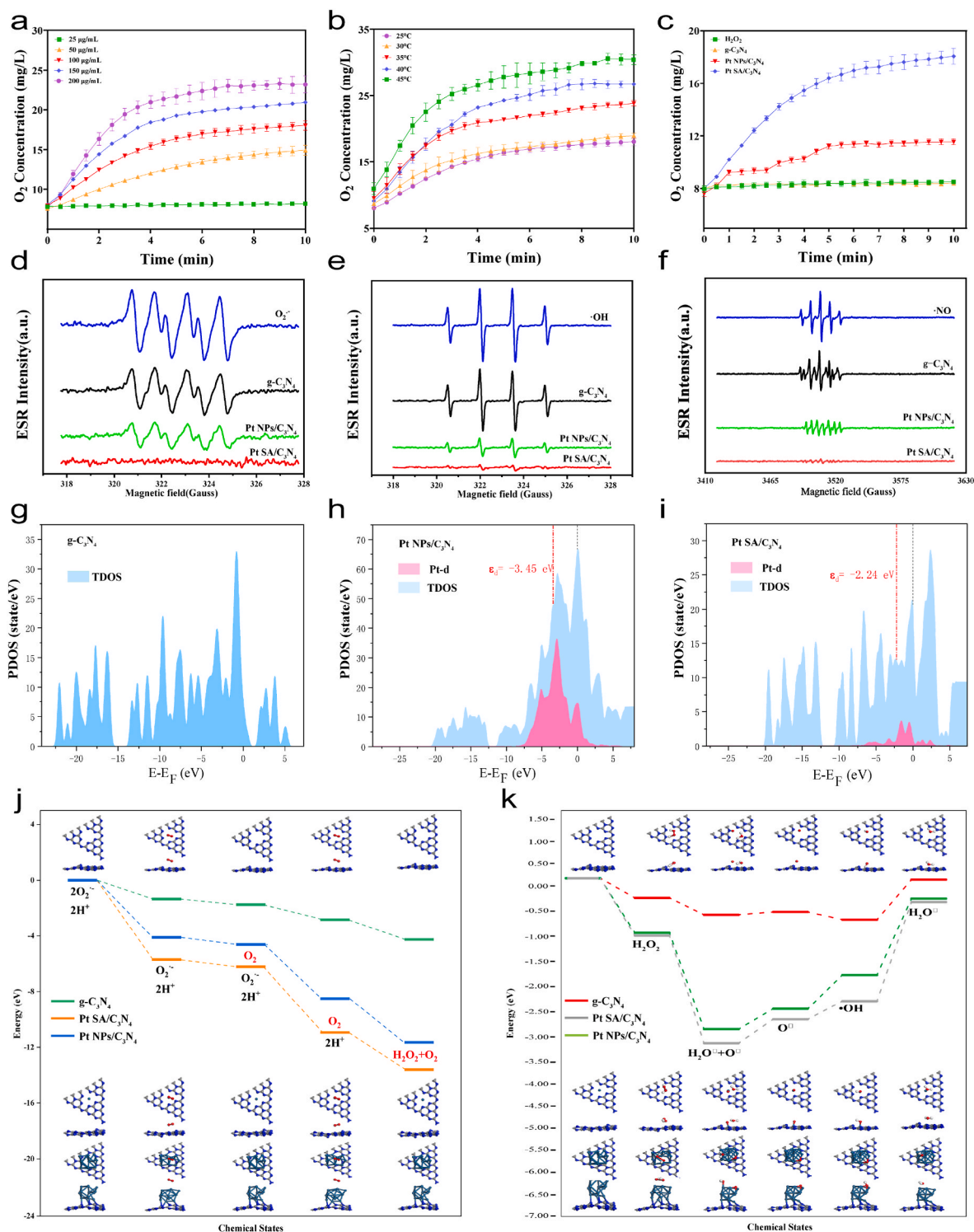


Fig. 3. SOD/CAT mimicking activity testing and DFT computations. (a, b) O₂ production employing the Pt SA/C₃N₄ nanozymes during H₂O₂ decomposition at different concentrations (a) and temperatures (b). (c) O₂ production employing the g-C₃N₄, Pt NPs/C₃N₄, and Pt SA/C₃N₄ nanozymes at the same concentrations during H₂O₂ decomposition. O₂^{•-} (d), •OH (e) and •NO (f) g-C₃N₄, Pt NPs/C₃N₄, and Pt SA/C₃N₄ nanozymes scavenging ascertained by ESR at equivalent concentrations. (g–h) Differential density of charge map and PDOS of g-C₃N₄ (g), Pt NPs/C₃N₄ (h) and Pt SA/C₃N₄ nanozymes (i). (j) Energy diagrams of the SOD-like catalytic reaction pathway of the Pt SA/C₃N₄ nanozymes, generated from DFT calculations. (k) DFT calculation-derived energy diagrams of the CAT-like catalytic reaction process of the Pt SA/C₃N₄ nanozyme. The data are expressed as the mean ± SD (n = 3).

scavenging free radicals, such as •OH and •NO, which are typical ROS, and its activity was significantly higher than those of g-C₃N₄ and Pt NPs/C₃N₄ (Fig. 3e and f).

2.3. DFT computational details

Density functional theory (DFT) studies were conducted to investigate the SOD and CAT processes in Pt SA/C₃N₄ in comparison with pure g-C₃N₄ and Pt NPs/C₃N₄ to understand the cause of the high SOD-like

and CAT-like catalytic efficiencies of Pt SA/C₃N₄. Based on the XAFS and XPS results, a 6-N-atom-coordinated Pt atom of the Pt SA/C₃N₄ model was constructed as the DFT calculation model. As shown in Fig. S13, from the differential charge density results of Pt SA/C₃N₄, we find that the electrons are transferred from the N atoms to the Pt atoms, further suggesting that the stability of the Pt–N₆ structure is beneficial for enzyme-catalysed reactions. The accumulation of electrons on the Pt

atom facilitates electron transfer from the Pt SA to O₂^{•-} or H₂O₂, thus leading to the degradation of O₂^{•-} or H₂O₂. Through the partial density of states (PDOS) analysis (Fig. 3g–i), compared with Pt NPs/C₃N₄, it can be observed that the d-band centre of Pt on Pt SA/C₃N₄ was closer to the Fermi level, which is beneficial for ROS adsorption.

Pt SA/C₃N₄ outperformed g-C₃N₄ and Pt NPs/C₃N₄ in catalysing O₂^{•-} into H₂O₂ and O₂ in this SOD-like reaction involving multiple chemical

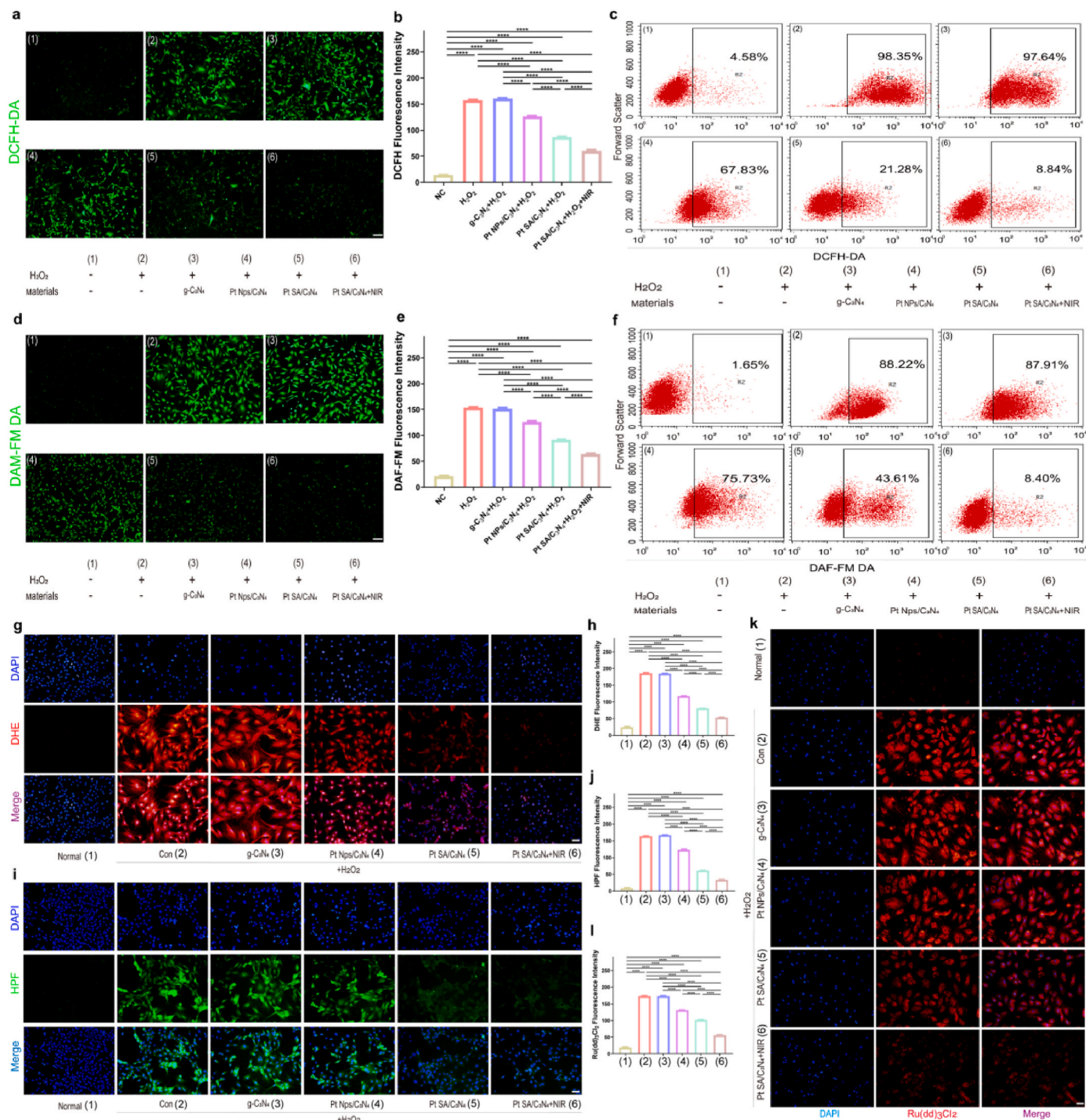


Fig. 4. Tests for scavenging reactive oxygen species (ROS) *in vitro* and the SOD/CAT-mimicking ability of Pt NPs/C₃N₄ nanozymes on chondrocytes that could be treated with enough H₂O₂ to cause excessive ROS production. (a) CLSM images of DCFH-DA, (b) Fluorescence quantification, (c) DCFH-DA flow cytometry (FCM) of chondrocytes. scale bar: 100 μm. (d) CLSM images of DAF-DA, (e) Fluorescence quantification, (f) DAF-DA flow cytometry (FCM) of chondrocytes. scale bar: 100 μm. CLSM images of DHE (g), HPF (i), and Ru(dpp)₃Cl₂ (k), respectively. Fluorescence quantification of DHE (h), HPF (j) and Ru(dpp)₃Cl₂ (i), respectively. scale bar: 50 μm. Data are expressed as mean ± SD (n = 3). Statistics were deemed significant if P < 0.05. (*P < 0.05, **P < 0.01, ***P < 0.001 and ****P < 0.0001).

states since the energy of the reaction catalysed by Pt SA/C₃N₄ was lower than that by g-C₃N₄ and Pt NPs/C₃N₄ in each step (Fig. 3j). The reaction energy for the first O₂⁻ degradation to free-oxygen molecules on the Pt SA/C₃N₄ catalyst was 4.47 eV more favourable than that on g-C₃N₄ and Pt NPs/C₃N₄, while it increased to 4.87 eV, which was more favourable for the second O₂⁻ degradation to H₂O₂. Therefore, the Pt-N₆ active sites of Pt SA/C₃N₄ exhibited superior SOD-like activity compared with those of g-C₃N₄ and Pt NPs/C₃N₄, consistent with the enzymatic activity test results.

The generation of H₂O₂ via SOD-like reactions induces oxidative stress. Interestingly, Pt SA/C₃N₄ mimicked CAT-like catalysis and decomposed H₂O₂ into H₂O and O₂ (Fig. 3k). In the CAT reaction, the adsorption energies of the Pt SA/C₃N₄ and Pt NPs/C₃N₄ towards the reactants and intermediates exhibited the same trend, whereas that of g-C₃N₄ were lower. According to the CAT reaction process, the second step of the surface O atom formation (H₂O₂→H₂O*+O*) is the rate determination step. The co-adsorption energy of the key intermediate species H₂O* and O* (-2.35 eV) on the Pt SA/C₃N₄ surface was lower than those in the cases of Pt NPs/C₃N₄ and g-C₃N₄, indicating that the route of H₂O₂ into O₂ and H₂O was the most favourable in the Pt SA/C₃N₄-mediated CAT-like catalysis process and that it had a significantly better CAT-like catalytic activity. Pt SA/C₃N₄ exhibited a higher adsorption energy than Pt NPs/C₃N₄ for the free radicals because the Pt d-band centre of Pt SA/C₃N₄ was closer to the Fermi level, which is consistent with the above results.

2.4. *In vitro* study of Pt SA/C₃N₄ nanozymes for scavenging intracellular ROS and alleviating oxidative stress

Interestingly, the Pt SAzyme exhibited outstanding photothermal conversion characteristics under NIR (808 nm) laser irradiation, similar to other monatomic nanozymes. The Pt SA/C₃N₄ nanozymes showed better photothermal stability, a higher rate of photothermal conversion, and a greater rise in temperature than the Pt NPs/C₃N₄ nanozymes (Figs. S14–17), and hardly produced ROS under 5 min laser irradiation (Figs. S18 and S19). Therefore, the photothermal effect of the Pt SA/C₃N₄ nanozymes activated by NIR can be further leveraged to improve their SOD- and CAT-like catalytic activities of Pt in the treatment of OA (Fig. S20).

The overproduction of ROS causes OA chondrocytes to undergo apoptosis and mitochondrial malfunction in addition to promoting inflammation, ultimately leading to OA progression. To verify the ROS scavenging and anti-inflammatory effects of the Pt SA/C₃N₄ nanozymes, we used H₂O₂-induced chondrocytes to simulate ROS-injured cartilage *in vitro*. The results showed slightly green fluorescence in the H₂O₂ group (Fig. 4a–c), which was significantly enhanced after being induced by H₂O₂, indicating the production of a large amount of ROS by H₂O₂. The fluorescence intensity of the g-C₃N₄ group was similar to that of the H₂O₂ group, indicating a weak scavenging effect on intracellular ROS. In contrast, the fluorescence intensity evidently decreased in both the Pt NPs/C₃N₄ and Pt SA/C₃N₄ groups. In particular, Pt SA/C₃N₄ exhibited the weakest fluorescence under NIR light irradiation, reaching a normal level, indicating effective ROS scavenging in H₂O₂-induced cells. In addition, Pt SA/C₃N₄ nanozymes hardly adsorbed proteins from physiological environments and were not affected by proteins for ROS clearance (Fig. S21). The results were further confirmed by an assay of intracellular free radicals, such as •NO (Fig. 4d–f), O₂•⁻ (Fig. 4g and h), •OH (Fig. 4i, j), and O₂ (Fig. 4k and l), using specific fluorescent probes. Thus, Pt SA/C₃N₄ nanozymes, particularly with the assistance of NIR light irradiation, can eliminate •NO, O₂•⁻, and •OH to reshape the cellular microenvironment, which is beneficial for alleviating the progression of OA.

2.5. Pt SA/C₃N₄ nanozymes repair mitochondrial function, reduce inflammatory response, and inhibit chondrocyte apoptosis

The Pt SA/C₃N₄ nanozymes have a special and efficient inhibitory effect on the oxidative stress, effectively scavenging large amounts of ROS and RNS from the OA cells. Live/dead staining and cell apoptosis flow cytometry detection have shown that Pt SA/C₃N₄ nanozymes can effectively inhibit cell apoptosis, and their effects can be further enhanced after NIR light irradiation. As shown in Fig. 5a–d, H₂O₂ induces a large amount of oxidative stress to kill chondrocytes, while the Pt SA/C₃N₄ nanozymes protect the cells from oxidative stress-induced death, resulting in a significant reduction in cell apoptosis (Fig. 5e; Fig. S22). The combination of NIR light irradiation and Pt SA/C₃N₄ nanozymes produced the strongest scavenging activity against ROS and RNS, which was beneficial for resisting chondrocyte apoptosis. The proportion of cell apoptosis produced was the lowest, and the higher the dose, the stronger the protective ability. In addition, the Pt SA/C₃N₄ nanozymes can be taken up by the chondrocytes and mitochondria due to its positive charge, and remain at the site of cartilage damage (Fig. S23).

We examined the effect of Pt SA/C₃N₄ nanozymes on the mitochondrial oxidative respiratory chain pathway and mitochondrial dysfunction to understand how these nanozymes shield chondrocytes from oxidative stress-induced cell damage (Fig. 5f, j). A strong green fluorescence, indicating an injured mitochondrial membrane, and a negligible red fluorescence, indicating a normal membrane, were observed in the chondrocytes of both the H₂O₂ and g-C₃N₄+H₂O₂ groups, suggesting complete damage to the mitochondrial membrane and a significant decrease in the mitochondrial membrane potential induced by H₂O₂. However, the red-to-green ratio was reversed after Pt NP/C₃N₄ or Pt SA/C₃N₄ administration. In particular, in the Pt SA/C₃N₄ + NIR group, the red-to-green ratio was the highest and close to that of the control group, indicating the effective recovery of the mitochondrial membrane damaged by H₂O₂. In addition, with the labelling of the intracellular calcium ions using the Flou-4 AM fluorescent probe, lower calcium ion levels were observed in the order of Pt SA/C₃N₄ + NIR < Pt SA/C₃N₄ < Pt NPs/C₃N₄ < g-C₃N₄, demonstrating that the Pt SA/C₃N₄ nanozymes could effectively reduce the influx of calcium ions into the chondrocytes to maintain the homeostasis of the intracellular calcium ions, thus ensuring the normal electrophysiological state of the chondrocyte membranes (Fig. 5g, k).

To clarify whether Pt SA/C₃N₄ nanozymes can effectively reduce the expression of inflammatory genes (IL-1β, IL-6, MMP13, and TNF-α), we investigated the gene expression using the qPCR method (Fig. 5n). The Pt SA/C₃N₄ nanozymes group exhibited lower levels of inflammatory factor expression than the H₂O₂ and g-C₃N₄+H₂O₂ groups. The decreased expression of these factors caused by H₂O₂ was reversed by treating with Pt NP/C₃N₄ and Pt SA/C₃N₄. Notably, Pt SA/C₃N₄ nanozymes had a better anti-inflammatory effect than clinical drugs (aspirin) (Figs. S24–25). Specifically, NIR-II irradiation increased the activity of the Pt SA/C₃N₄ nanozymes, leading to a dramatic decrease in the expression of inflammatory markers, which reached close to normal levels. Immunofluorescence staining for inflammatory factors (MMP-13 and IL-6) also confirmed these results, with negative staining observed in the Pt SA/C₃N₄ group (Fig. 5h, i, l, m). Furthermore, we detected changes in the expression of CAT, whereas SOD exhibited an same trend. The Pt SA/C₃N₄ nanozymes, particularly under NIR light irradiation, upregulated the expression of CAT and SOD, which were the most prominent antioxidant factors in all the groups (Fig. 5o). These results indicate that with the aid of NIR light irradiation, Pt SA/C₃N₄ nanozymes can not only reduce inflammatory factors but also upregulate intracellular antioxidant factors and cartilage markers, which is promising for delaying the progression of OA inflammation.

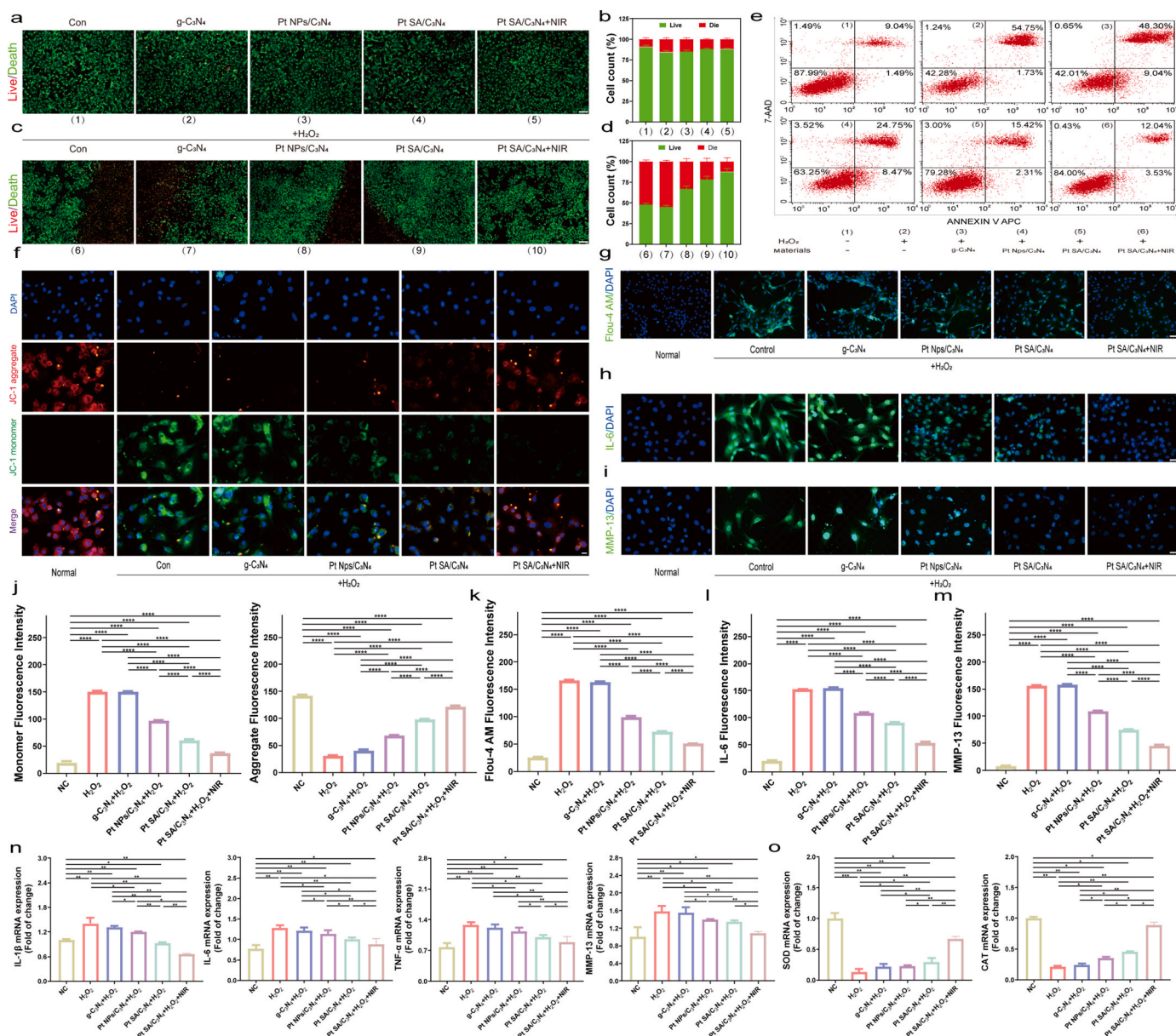


Fig. 5. The mechanism of Pt SA/C₃N₄ nanozymes ROS scavenging for shielding chondrocytes from apoptosis and inflammatory erosion is explored. (a, c) CLSM image of Calcein/PI staining of chondrocytes, calcein (green) stained live and PI (red) stained dead cells, scale bar: 200 μm. (b) Fluorescence quantification for (a), (d) Fluorescence quantification for (c). (e) FCM patterns of chondrocytes following various treatments that were stained with V-APC/7-ADD. (f) CLSM image of JC-1 membrane potential detection, scale bars: 50 μm. (g) CLSM images of Fluor-4 AM and (k) Fluorescence quantification. scale bars: 100 μm. After varying treatments, chondrocytes labeled with MMP-13 and IL-6 fluorescent antibodies were subjected to CLSM images (h–i) and qualitative data (l–m). scale bar: 100 μm. (n) Relative inflammatory factor RNA expression levels in chondrocytes. (o) Relative anti-inflammatory factor RNA expression levels in chondrocytes. Data are expressed as mean ± SD (n = 3). Statistics were deemed significant if P < 0.05. (*P < 0.05, **P < 0.01, ***P < 0.001 and ****P < 0.0001).

2.6. Pt SA/C₃N₄ treats arthritis by rescuing the oxidative phosphorylation pathway

To investigate the molecular mechanism of Pt SA/C₃N₄ in alleviating arthritis, we performed RNA sequencing of normal chondrocytes (NC group), OA chondrocytes (OA group), and OA chondrocytes treated with Pt SA/C₃N₄ (Pt SA/C₃N₄ group). The results showed that there were 7733 differentially expressed genes (DEGs) (p < 0.05) in the OA vs. NC group with 6072 upregulated and 1661 downregulated genes (Fig. 6a). However, there were only 458 DEGs (p < 0.05) in Pt SA/C₃N₄ vs OA, in which 251 genes were upregulated and 207 genes were downregulated (Fig. 6b). The gene set enrichment analysis (GSEA) for OA vs NC showed that 7733 DEGs were significantly enriched in 34 signalling paths (qvalues < 0.05, NES > |±1|). In the 12 enriched pathways with the

highest and lowest NES (Fig. 6c), the NES of the oxidative phosphorylation pathway scored the second lowest (NES = -3.47), indicating that the DEGs of OA vs NC enriched in the oxidative physiology pathway were significantly downregulated. The KEGG enrichment analysis of the DEGs of Pt SA/C₃N₄ vs OA also confirmed a significantly enriched oxidative phosphorylation pathway (Fig. 6d), which overlapped with that of OA vs. NC. Thus, we speculate that oxidative phosphorylation is dysregulated in OA, which is also regulated by Pt SA/C₃N₄.

We investigated the DEGs that were enriched in the oxidative phosphorylation pathways in OA vs. NC and Pt SA/C₃N₄ vs OA. We found that MT-ATP6 was downregulated in OA (Fig. 6e) but was rescued by Pt SA/C₃N₄ (Fig. 6f). During oxidative phosphorylation, MT-ATP6 is a component of the F0 of ATP synthase [34], which participates in the catalysed production of ATP [35]. therefore, Pt SA/C₃N₄ may alleviate

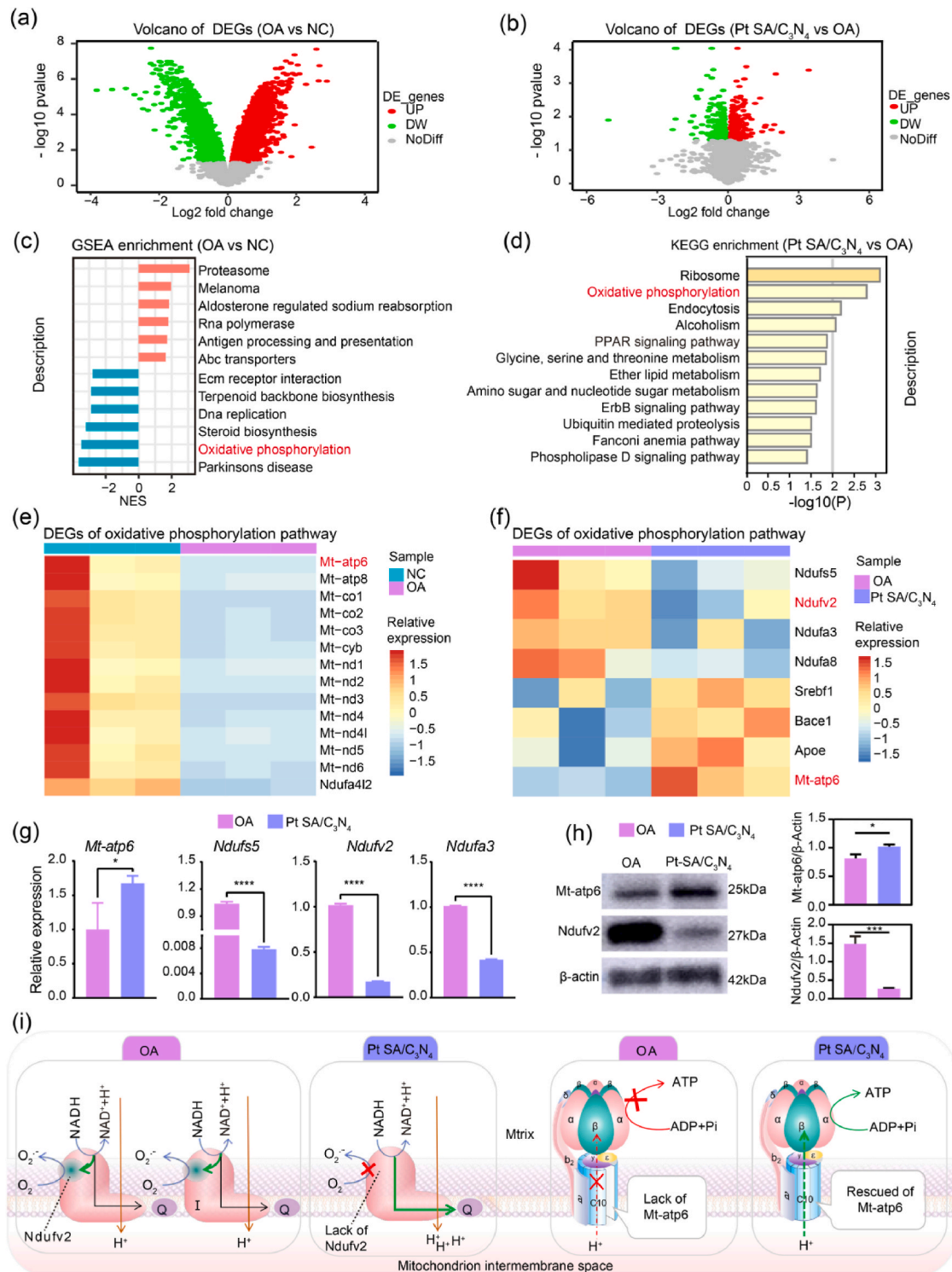


Fig. 6. (a) The volcano plot showed the DEGs of OA_vs_NC. (b) The volcano plot showed the DEGs of Pt SA/C₃N₄_vs_OA. (c) The GSEA enrichment result of the DEGs of OA_vs_NC. (d) The KEGG enrichment result of the DEGs of Pt SA/C₃N₄_vs_OA. (e) DEGs of both OA_vs_NC and oxidative phosphorylation pathway. (f) DEGs of both Pt SA/C₃N₄_vs_OA and oxidative phosphorylation pathway. (g) The qRT-PCR reveals the genes expression of MT-ATP6, NDUFS5, NDUFV2 and NDUF3. (h) The western-blot reveals the protein expression of MT-ATP6 and NDUFV2, and their statistical result. (i) The potential mechanism of Pt SA/C₃N₄ in Treating OA. Complex I is an important biological macromolecule that produces ROS, Pt SA/C₃N₄ downregulates its composition to reduce its quantity, thereby reducing ROS production. Additionally, Pt SA/C₃N₄ reduces electron transfer to the direction of ROS production by reducing NDUFV2. In the lack of NDUFV2, electrons prefer to transfer to the coenzyme Q, resulting in more efficient H⁺ pumping to the mitochondrial intermembrane space. The H⁺ proton gradient can drive normal ATP synthase synthesis of ATP. However, in OA, the MT-ATP6 component of ATP synthase F₀ is insufficient, resulting in the loss of proton pump function. Pt SA/C₃N₄ rescued MT-ATP6 and restored the function of ATP synthase to synthesize ATP. Data are expressed as mean \pm SD (n = 3). Statistics were deemed significant if P < 0.05. (*P < 0.05, **P < 0.01, ***P < 0.001 and ****P < 0.0001).

OA by regulating MT-ATP6 to rescue the ATP synthase activity. In the oxidative phosphorylation pathway of Pt SA/C₃N₄ versus OA, Pt SA/C₃N₄ downregulated the expression of NDUFS5, NDUFV2, and NDUFA3 (Fig. 6f). NDUFS5, NDUFV2, and NDUFA3 are the components of complex 1, which is one of the important sites for ROS production [36–38]. Thus, Pt SA/C₃N₄ may reduce the synthesis of complex 1 by reducing its components, thereby reducing ROS production. A reported mechanism is that the electrons transferred from NADH are accepted by complex 1 and transmitted through two pathways. The first electron transfer pathway is from FMN to NDUFV2, which reduces oxygen (O₂) to superoxide free radicals (O₂⁻), which causes ROS production [39]. The other electron transfer pathway is from FMN to coenzyme Q, which can pump H⁺ protons between the inner and outer mitochondrial membranes, thereby establishing a transmembrane proton gradient. The proton gradient drives H⁺ back to the mitochondrial matrix through ATP synthase to drive the synthesis of ATP. Thus, Pt SA/C₃N₄ downregulates the NDUFV2 components that produce superoxide anions in complex 1, which may enable the transfer of more electrons toward ATP production (Fig. S26).

Finally, we further verified the expression of key genes by qPCR, including MT-ATP6, NDUFS5, NDUFV2, and NDUFA3, (Fig. 6g). Furthermore, the key protein expression levels of MT-ATP6 and NDUFV2 were verified using western blotting (Fig. 6h, Fig. S27, Fig. S28). This mechanism is summarised in Fig. 6i. In summary, Pt SA/C₃N₄ regulates the expression of mitochondrial respiratory chain complexes, mainly NDUFV2 of complex 1 and MT-ATP6 of ATP synthase, to reduce ROS and rescue ATP production.

2.7. Intraarticularly administration of Pt SA/C₃N₄ nanozymes as an *in vivo* treatment for OA

To evaluate whether Pt SA/C₃N₄ nanozymes can inhibit the progression of OA *in vivo*, we constructed a rat OA joint model using anterior cruciate ligament transection (ACLT) (Fig. 7a). The high dispersibility of Pt SA/C₃N₄ nanozymes in the physiological environment (Fig. S29) and their stable enzyme activity in synovial fluid ensured that they can be injected into the joint cavity *in vivo* for the treatment of OA. After the successful construction of the OA joint model, we evaluated the photothermal efficacy of the Pt SA/C₃N₄ nanozymes after injecting them into the joint cavity.

The results showed that the Pt SA/C₃N₄ nanozymes exhibited a good photothermal performance (Fig. S30). After four and eight weeks of treatment, the knee joints of the rats were collected for evaluation. Macroscopic observations of the femoral and tibial joint surfaces of the joints showed severe cartilage surface damage, such as lesions and erosion, in the saline group, which deteriorated over time, indicating the successful establishment of the OA model. The cartilage damage was gradually recovered after treatment with Pt NPs/C₃N₄ and Pt SA/C₃N₄. In particular, the cartilage surface was smooth and glossy after Pt SA/C₃N₄+NIR treatment, which was similar to the normal cartilage in the sham group (Fig. 7b, Fig. S31). Macroscopic scores also confirmed the results of the macroscopic observations (Fig. 7c). The Pt SA/C₃N₄+NIR score was nearly identical to that of the sham group. Notably, Pt SA/C₃N₄ nanozymes had a more effective therapeutic effect than clinical aspirin. (Fig. S32).

To further confirm the role of the Pt SA/C₃N₄ nanozymes in reducing joint inflammation and cartilage damage, we performed pathological staining and analysis. HE (Fig. 7f, Fig. S33) and safranin staining (Fig. 7e, Fig. S34) of the rat knee joint produced the most severe cartilage damage in the saline group, as evidenced by fibrillated lesions, cell clusters, and proteoglycan loss. However, after treatment with the Pt SA/C₃N₄ nanozymes, the surface of the cartilage showed a significant reversal of surface fibrosis, prevention of proteoglycan loss, and suppression of severe cartilage erosion, which were superior to those of the g-C₃N₄ and Pt NPs/C₃N₄ groups. The cartilage resembled that of the sham surgery group, particularly after the combined NIR light

irradiation. The Pt SA/C₃N₄ and Pt SA/C₃N₄+NIR scores were low and approached those of the sham surgery group after quantification using the Mankin cartilage scoring standard (Fig. 7h). This finding further supports the idea that the Pt SA/C₃N₄ nanozymes in combination with NIR II can have a significant therapeutic effect on OA. Synovial HE staining further demonstrated that the treatment with the Pt SA/C₃N₄ nanozymes reduced the density of the synovial lining cell layer and resident cell layer more evidently than the other treatment groups, suggesting their potential to alleviate synovial inflammation (Fig. 7d, e, S35). To verify the effect of Pt SA/C₃N₄ on the inflammatory response, we performed immunohistochemistry and immunofluorescence analyses to investigate the expression of the inflammatory markers IL-6 and MMP-13. As shown in Fig. 7i–n and Figs. S36–37, the almost negative staining in contrast to the OA group suggests that Pt SA/C₃N₄ significantly reduced the expressions of IL-6 and MMP-13, particularly under NIR-II irradiation, and these results were close to the sham group.

Further, Pt SA/C₃N₄ nanozymes were labeled with Cy5 fluorescent probes for live imaging in an SD rat model to assess the stability of the nanozymes *in vivo* (Fig. S38). After injection of Pt SA/C₃N₄ nanozymes into the knee joint, the fluorescence intensity gradually decrease after 24 h and vanishes entirely after 120 h. Notably, the fluorescence signal intensity in the kidney, bladder, and colon was higher, suggesting that renal and hepatic routes can facilitate the clearance of Pt SA/C₃N₄ nanozymes (Fig. S39). We evaluated the biological safety of the Pt SA/C₃N₄ nanozymes *in vivo* by conducting haemolysis experiments (Fig. S40). The results showed that haemolysis hardly occurred within a certain nanozyme concentration range. After the Pt SA/C₃N₄ nanozyme treatment, no histopathological abnormalities or lesions were observed in the HE staining of the rat organs, and the Pt content in the organs was extremely low (Fig. 8a and b). Furthermore, blood routine and biochemical tests showed that after Pt SA/C₃N₄ nanozyme treatment, indicators, such as the red blood cell count, white blood cell count, haemoglobin, uric acid, creatine kinase, total protein, aspartate transaminase, and alanine transaminase levels, were within the normal range, similar to those of the saline group (Fig. 8c–p). Thus, it can be concluded that the Pt SA/C₃N₄ nanozymes have favourable biosafety properties and therapeutic effect in the treatment of OA.

3. Conclusions

In this study, we innovatively designed g-C₃N₄-supported Pt SA catalysts as SOD/CAT mimics with an enzymatic activity that is tunable under NIR light irradiation to scavenge ROS/RNS and regulate mitochondrial ATP production, ultimately to delay the progression of OA. Ligand-mediated strategies were utilised to chelate Pt⁴⁺, followed by π - π interaction with the modified g-C₃N₄, to prepare high-loading Pt SA nanozymes. XAS and XPS analyses revealed that the Pt-N₆ active centres in Pt SA/C₃N₄ formed electron capture sites for the electron holes, and the N-rich sites of g-C₃N₄ transferred electrons to Pt, thus enhancing metal-carrier interactions. DFT calculations demonstrated that g-C₃N₄ regulated the d-band centre of Pt, and Pt SA/C₃N₄ had a higher adsorption energy for free radicals than g-C₃N₄ and Pt NPs/C₃N₄, which was beneficial for reducing the reaction energy barrier and thus improving the SOD/CAT reaction. NIR light irradiation was used to modulate the catalytic activity of Pt SA/C₃N₄ via photothermal conversion. Based on the use of H₂O₂-induced chondrocytes to simulate ROS-injured cartilage *in vitro* and a joint model of the OA, we demonstrated that Pt SA/C₃N₄, particularly under NIR II irradiation, could effectively scavenge ROS/RNS, reduce oxidative stress-induced damage, protect mitochondrial function, inhibit the inflammatory response, and further rebuild the OA microenvironment, ultimately delaying the progression of OA. The bioinformatic analysis indicated that Pt SA/C₃N₄ regulated the expression of mitochondrial respiratory chain complexes, mainly NDUFV2 of complex 1 and MT-ATP6 of ATP synthase, to reduce ROS and rescue the ATP energy crisis.

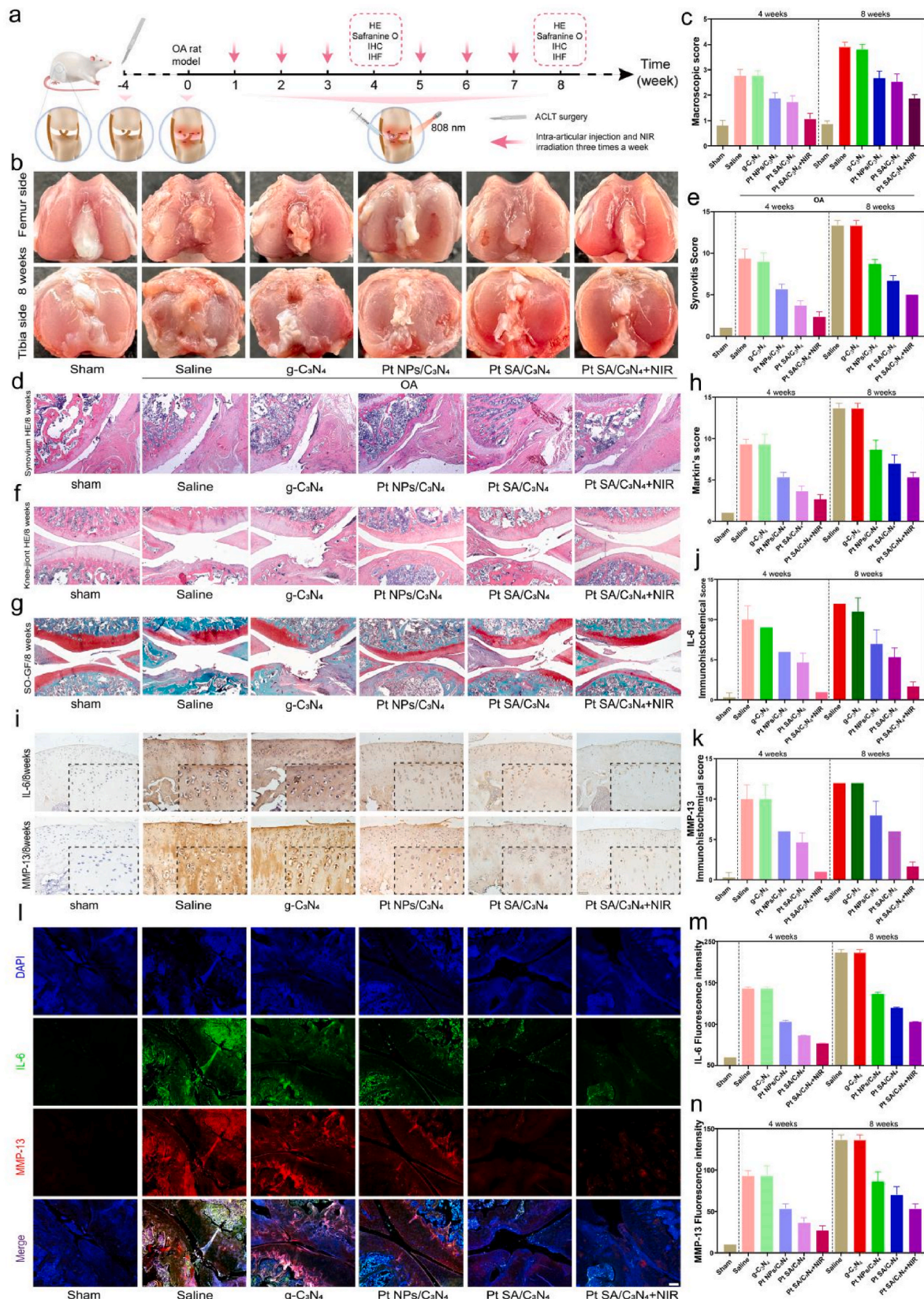


Fig. 7. *In vivo* OA mitigation tests based on Pt SA/C₃N₄ nanozymes scavenging of ROS. (a) Procedure schematic of *in vivo* OA mitigation using g-C₃N₄, Pt NPs/C₃N₄ and Pt SA/C₃N₄ nanozymes. (b) General views of the knee joint obtained from SD rats and (c) macroscopic rating. (d) Synovium HE staining and (e) synovium score. (f) knee-joint HE staining. (g) Saffron-O and Fast Green staining, (h) Markin's score. (i) Optical image of immunohistochemistry, (j–k) Immunohistochemical quantification. scale bars: 200 μm for d, f, g and i. (l) CLSM images of MMP-13 and IL-6 in different groups and (n) Fluorescence quantification level. scale bars: 200 μm. Data are expressed as mean ± SD (n = 3). Statistics were deemed significant if P < 0.05. (*P < 0.05, **P < 0.01, ***P < 0.001 and ****P < 0.0001).

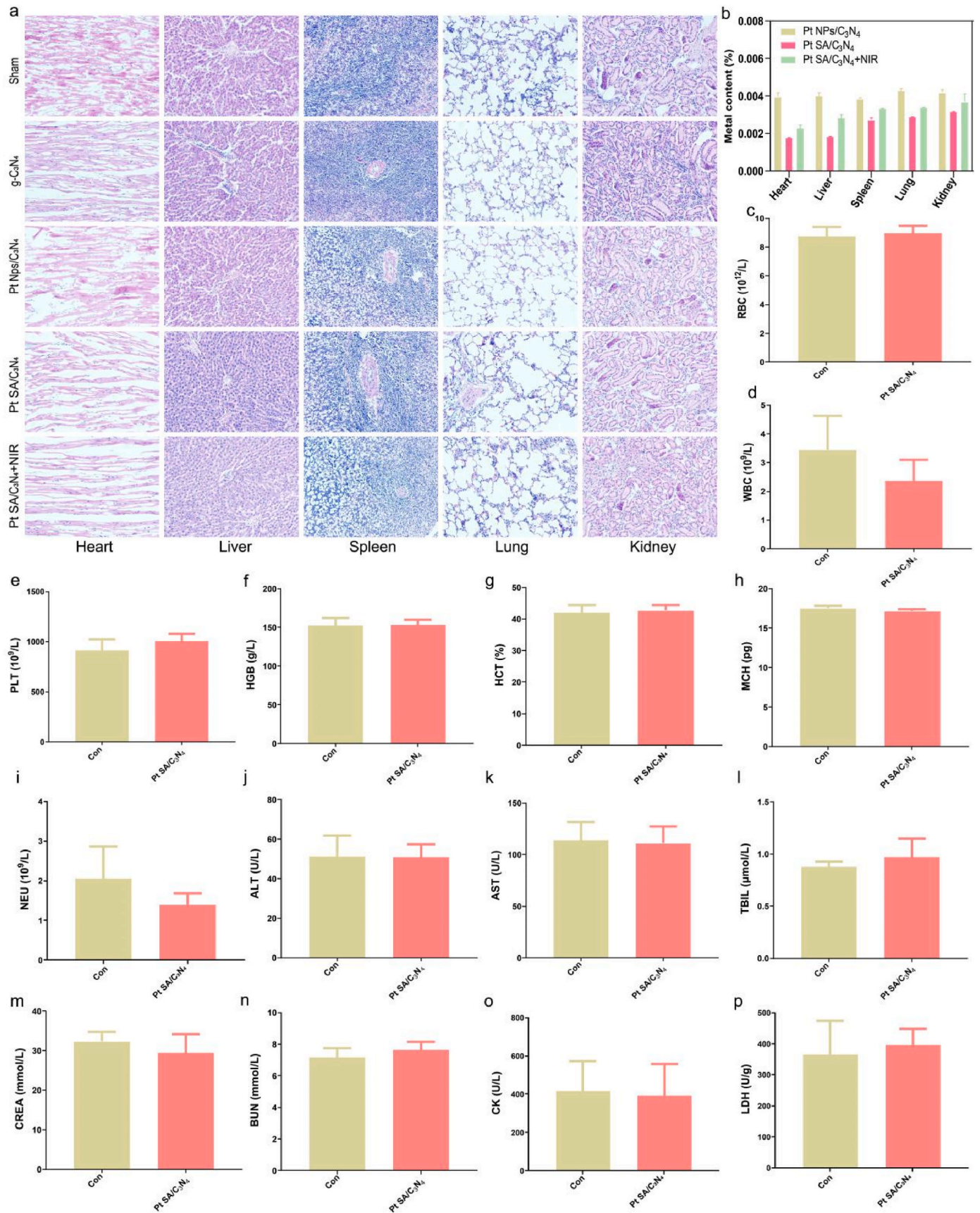


Fig. 8. Biosafety evaluation of Pt SA/C₃N₄ nanozymes *in vivo*. (a) HE images of main visceral organs in different groups of rats, scale bar: 100 μm. (b) Pt concentrations in various organs taken from SD rats exposed to Pt SA/C₃N₄ nanozymes. (c–p) Blood routine and blood biochemistry after Pt SA/C₃N₄ nanozymes treatments. Data are expressed as mean ± SD (n = 3).

Ethics approval and consent to participate

The Guangxi Medical University Animal Research Ethics Committee's guiding principles (Protocol Number: 202204012) were followed in all experiments.

Declaration of competing interest

The authors declare no competing interests.

CRediT authorship contribution statement

Jianhui Xiang: Writing – original draft, Software, Methodology, Investigation, Formal analysis, Data curation. **Xin Yang:** Writing – original draft, Software, Formal analysis, Data curation. **Manli Tan:** Writing – original draft, Software, Conceptualization. **Jianfeng Guo:** Formal analysis. **Yuting Ye:** Formal analysis. **Jiejia Deng:** Formal analysis. **Zhangrui Huang:** Formal analysis. **Hanjie Wang:** Formal analysis. **Wei Su:** Formal analysis. **Jianwen Cheng:** Funding acquisition. **Li Zheng:** Writing – review & editing, Funding acquisition. **Sijia Liu:** Funding acquisition. **Jingping Zhong:** Writing – review & editing, Funding acquisition, Conceptualization. **Jinmin Zhao:** Funding acquisition.

Acknowledgements

The authors acknowledge the support from the Guangxi Natural Science Foundation (No. 2023GXNSFBA026020), Guangxi Scientific Research and Technological Development Foundation (Grant No. GuikeAB21220062), National Natural Science Foundation of China (Grant No. 82160429, 82360426, 52301303, 81960400).

Appendix A. Supplementary data

Supplementary data to this article can be found online at <https://doi.org/10.1016/j.bioactmat.2024.02.018>.

References

- [1] K. Lu, Q. Wang, L. Hao, G. Wei, T. Wang, W.W. Lu, G. Xiao, L. Tong, X. Zhao, D. Chen, miR-204 ameliorates osteoarthritis pain by inhibiting SP1-LRP1 signaling and blocking neuro-cartilage interaction, *Bioact. Mater.* 26 (2023) 425–436.
- [2] S. Muthu, J.V. Korpershoek, E.J. Novais, G.F. Tawy, A.P. Hollander, I. Martin, Failure of cartilage regeneration: emerging hypotheses and related therapeutic strategies, *Nat. Rev. Rheumatol.* 19 (7) (2023) 403–416.
- [3] O.H. Jeon, C. Kim, R.-M. Laberge, M. Demaria, S. Rathod, A.P. Vasserot, J. W. Chung, D.H. Kim, Y. Poon, N. David, et al., Local clearance of senescent cells attenuates the development of post-traumatic osteoarthritis and creates a pro-regenerative environment, *Nat. Med.* 23 (6) (2017) 775–781.
- [4] Y. Zhao, T. Huang, X. Zhang, Y. Cui, L. Zhang, L. Li, Z. Wang, Piezotronic and piezo-phototronic effects on sonodynamic disease therapy, *BMEMat* 1 (1) (2023) e12006.
- [5] M.Y. Ansari, N.M. Khan, I. Ahmad, T.M. Haqqi, Parkin clearance of dysfunctional mitochondria regulates ROS levels and increases survival of human chondrocytes, *Osteoarthr. Cartilage* 26 (8) (2018) 1087–1097.
- [6] S. Guan, L. Zhao, R. Peng, Mitochondrial respiratory chain supercomplexes: from structure to function, *Int. J. Mol. Sci.* 23 (22) (2022), 1422–0067.
- [7] D. Nolfi-Donegan, A. Braganza, S. Shiva, Mitochondrial electron transport chain: oxidative phosphorylation, oxidant production, and methods of measurement, *Redox Biol.* 37 (2020) 101674.
- [8] P. Yu, Y. Li, H. Sun, H. Zhang, H. Kang, P. Wang, Q. Xin, C. Ding, J. Xie, J. Li, Mimicking antioxidant and Hyaluronan synthase: a zwitterionic nanozyme for photothermal therapy of osteoarthritis, *Adv. Mater.* 35 (44) (2023) 2303299.
- [9] H. Lu, J. Wei, K. Liu, Z. Li, T. Xu, D. Yang, Q. Gao, H. Xiang, G. Li, Y. Chen, Radical-scavenging and subchondral bone-regenerating nanomedicine for osteoarthritis treatment, *ACS Nano* 17 (6) (2023) 6131–6146.
- [10] W. Wang, J. Duan, W. Ma, B. Xia, F. Liu, Y. Kong, B. Li, H. Zhao, L. Wang, K. Li, et al., Trimanganese tetroxide nanozyme protects cartilage against degeneration by reducing oxidative stress in osteoarthritis, *Adv. Sci.* 10 (17) (2023) 2205859.
- [11] R. Zeng, W. Wang, G. Cai, Z. Huang, J. Tao, D. Tang, C. Zhu, Single-atom platinum nanocatalyst-improved catalytic efficiency with enzyme-DNA supermolecular architectures, *Nano Energy* 74 (2020) 104931.
- [12] S. Cupini, S. Di Marco, L. Boselli, A. Cavalli, G. Tarricone, V. Mastronardi, V. Castagnola, E. Colombo, P.P. Pompa, F. Benfenati, Platinum nanozymes counteract photoreceptor degeneration and retina inflammation in a light-damage model of age-related macular degeneration, *ACS Nano* (2023), 1936–0851.
- [13] Y. Li, K.-H. Yun, H. Lee, S.-H. Goh, Y.-G. Suh, Y. Choi, Porous platinum nanoparticles as a high-Z and oxygen generating nanozyme for enhanced radiotherapy in vivo, *Biomaterials* 197 (2019) 12–19.
- [14] B.L. Oliveira, Z. Guo, G.J.L. Bernardes, Inverse electron demand Diels-Alder reactions in chemical biology, *Chem. Soc. Rev.* 46 (16) (2017) 4895–4950.
- [15] L. Zhang, K. Doyle-Davis, X. Sun, Pt-Based electrocatalysts with high atom utilization efficiency: from nanostructures to single atoms, *Energy Environ. Sci.* 12 (2) (2019) 492–517.
- [16] Y. Pei, W. Zhu, R. Yue, L. Wang, R. Li, J. Zhang, Y. Yin, Controllable construction of Pt/CNT catalyst layers to improve the Pt utilization in PEMFC, *J. Mater. Chem. A* (2023) 2050–7488.
- [17] Y. Zhu, Y. Liao, J. Zou, J. Cheng, Y. Pan, L. Lin, X. Chen, Engineering single-atom nanozymes for catalytic biomedical applications, *Small* 19 (30) (2023) 2300750.
- [18] K. Kim, J. Lee, O.K. Park, J. Kim, D. Lee, V.K. Paidi, E. Jung, H.S. Lee, B. Lee, et al., Geometric tuning of single-atom FeN₄ sites via edge-generation enhances multi-enzymatic properties, *Adv. Mater.* 35 (19) (2023) 2207666.
- [19] J. Ye, W. Lv, C. Li, S. Liu, X. Yang, J. Zhang, C. Wang, J. Xu, G. Jin, B. Li, et al., Tumor response and NIR-II photonic thermal Co-enhanced catalytic therapy based on single-atom manganese nanozyme, *Adv. Funct. Mater.* 32 (47) (2022) 2206157.
- [20] X. Zhang, G. Li, G. Chen, D. Wu, X. Zhou, Y. Wu, Single-atom nanozymes: a rising star for biosensing and biomedicine, *Coord. Chem. Rev.* 418 (2020) 213376.
- [21] G.F.S.R. Rocha, M.A.R. da Silva, A. Rogolino, G.A.A. Diab, L.F.G. Noleto, M. Antonietti, I.F. Teixeira, Carbon nitride based materials: more than just a support for single-atom catalysis, *Chem. Soc. Rev.* 52 (15) (2023) 4878–4932.
- [22] L. Shi, C. Wu, Y. Wang, Y. Dou, D. Yuan, H. Li, H. Huang, Y. Zhang, I.D. Gates, X. Sun, et al., Rational design of coordination bond connected metal organic frameworks/MXene hybrids for efficient solar water splitting, *Adv. Funct. Mater.* 32 (30) (2022) 2202571.
- [23] C. Hu, W.-Z. Hung, M.-S. Wang, P.-J. Lu, Phosphorus and sulfur codoped g-C₃N₄ as an efficient metal-free photocatalyst, *Carbon* 127 (2018) 374–383.
- [24] J. Xu, M. Antonietti, The performance of nanoparticulate graphitic carbon nitride as an amphiphile, *J. Am. Chem. Soc.* 139 (17) (2017) 6026–6029.
- [25] J. Liu, Y. Zhang, L. Zhang, F. Xie, A. Vasileff, S.-Z. Qiao, Graphitic carbon nitride (g-C₃N₄)-derived N-rich graphene with tuneable interlayer distance as a high-rate anode for sodium-ion batteries, *Adv. Mater.* 31 (24) (2019) 1901261.
- [26] Y. Guo, B. Qiao, Atom-by-atom fabrication of metal clusters for efficient selective hydrogenation, *Sci. China: Chem.* 65 (2) (2022) 202–203.
- [27] E. Vorobyeva, Z. Chen, S. Mitchell, R.K. Leary, P. Midgley, J.M. Thomas, R. Hauert, E. Fako, N. López, J. Pérez-Ramírez, Tailoring the framework composition of carbon nitride to improve the catalytic efficiency of the stabilised palladium atoms, *J. Mater. Chem. A* 5 (31) (2017) 16393–16403.
- [28] X. Liu, S. Wang, W. Yu, J. Zhang, S. Fang, J. Zhang, J. Qiu, F. Kong, X. Duan, Single platinum atoms anchored on holy carbon nitride for efficient photodegradation of sulfonyleurea herbicide, *Chem. Eng. J.* 446 (2022) 137426.
- [29] L. Shi, S. Liu, Z. He, Construction of Sn/oxide g-C₃N₄ nanostructure by electrostatic self-assembly strategy with enhanced photocatalytic degradation performance, *Appl. Surf. Sci.* 457 (2018) 1035–1043.
- [30] Q. Wu, H. Zhang, H. Liu, External physical field-driven nanocatalytic cancer therapy, *BMEMat* 1 (1) (2023) e12010.
- [31] S. Roy, Z. Li, Z. Chen, A.C. Mata, P. Kumar, S.C. Sarma, I.F. Teixeira, I.F. Silva, G. Gao, N.V. Tarakina, et al., Cooperative copper single atom catalyst in two-dimensional carbon nitride for enhanced CO₂ electrolysis to methane, *Adv. Mater.* 65 (2) (2023) 1869–1870.
- [32] C. Ding, X. Lu, B. Tao, L. Yang, X. Xu, L. Tang, H. Chi, Y. Yang, D.M. Meira, L. Wang, et al., Interlayer spacing regulation by single-atom Indium⁶⁺-N₄ on carbon nitride for boosting CO₂/CO photo-conversion, *Adv. Funct. Mater.* 33 (35) (2023) 2302824.
- [33] X.-H. Jiang, L.-S. Zhang, H.-Y. Liu, D.-S. Wu, F.-Y. Wu, L. Tian, L.-L. Liu, J.-P. Zou, S.-L. Luo, B.-B. Chen, Silver single atom in carbon nitride catalyst for highly efficient photocatalytic hydrogen evolution, *Angew. Chem., Int. Ed.* 59 (51) (2020) 23112–23116.
- [34] Y. Lai, Y. Zhang, S. Zhou, J. Xu, Z. Du, Z. Feng, L. Yu, Z. Zhao, W. Wang, Y. Tang, et al., Structure of the human ATP synthase, *Mol. Cell* 83 (12) (2023) 2137–2147, 2134.
- [35] G. Manfredi, J. Fu, J. Ojaimi, J.E. Sadlock, J.Q. Kwong, J. Guy, E.A. Schon, Rescue of a deficiency in ATP synthesis by transfer of MTATP6, a mitochondrial DNA-encoded gene, to the nucleus, *Nat. Genet.* 30 (4) (2002) 394–399.
- [36] J. Zhu, K.R. Vinothkumar, J. Hirst, Structure of mammalian respiratory complex I, *Nature* 536 (7616) (2016) 354–358.
- [37] L. Kussmaul, J. Hirst, The mechanism of superoxide production by NADH: ubiquinone oxidoreductase (complex I) from bovine heart mitochondria, *P. Natl. Acad. Sci. USA.* 103 (20) (2006) 7607–7612.
- [38] M. Vranas, D. Wohlwend, D. Qiu, S. Gerhardt, C. Trncik, M. Pervaiz, K. Ritter, S. Steimle, A. Randazzo, O. Einsle, et al., Structural basis for inhibition of ROS-producing respiratory complex I by NADH-OH, *Angew. Chem., Int. Ed.* 60 (52) (2021) 27277–27281.
- [39] N. Mota-Martorell, M. Jove, I. Pradas, I. Sanchez, J. Gómez, A. Naudi, G. Barja, R. Pamplona, Low abundance of NDUFB2 and NDUFS4 subunits of the hydrophilic complex I domain and VDAC1 predicts mammalian longevity, *Redox Biol.* 34 (2020) 101539.